Radiology

Henkjan J. Huisman, MS, PhD
Jurgen J. Fütterer, MD
Emile N. J. T. van Lin, MD
Arjan Welmers, MD
Tom W. J. Scheenen, MS, PhD
Jorn A. van Dalen, MS, PhD
Andries G. Visser, MS, PhD
J. A. Witjes, MD, PhD
Jelle O. Barentsz, MD, PhD

Published online before print
10.1148/radiol.2361040560
Radiology 2005; 236:311–317

Abbreviations:
DIL = dominant intraprostatic lesion
ICP = iterative closest point
IMRT = intensity-modulated radiation therapy
3D = three-dimensional

[1] From the Departments of Radiology (H.J.H., J.J.F., A.W., T.W.J.S., J.A.v.D., J.O.B.), Radiotherapy (E.N.J.T.v.L., A.G.V.), and Urology (J.A.W.), Radboud University Nijmegen Medical Center, Geert Grooteplein zuid 10, NL 6500 HB, Nijmegen, the Netherlands. Received March 26, 2004; revision requested June 8; revision received August 20; accepted October 1. **Address correspondence to** H.J.H. (e-mail: *h.huisman@rad.umcn.nl*).

Authors stated no financial relationship to disclose.

Author contributions:
Guarantors of integrity of entire study, all authors; study concepts, all authors; study design, A.W., J.O.B., H.J.H.; literature research, J.A.v.D., H.J.H.; clinical and experimental studies, A.W., J.J.F., J.O.B.; data acquisition, A.W., J.J.F., J.O.B., T.W.J.S.; data analysis/interpretation, H.J.H., J.A.v.D., T.W.J.S.; statistical analysis, H.J.H., J.A.v.D.; manuscript preparation, H.J.H.; manuscript definition of intellectual content, all authors; manuscript editing, H.J.H.; manuscript revision/review and final version approval, all authors

Prostate Cancer: Precision of Integrating Functional MR Imaging with Radiation Therapy Treatment by Using Fiducial Gold Markers[1]

The use of intensity-modulated radiation therapy for treatment of dominant intraprostatic lesions may require integration of functional magnetic resonance (MR) imaging with treatment-planning computed tomography (CT). The purpose of this study was to compare prospectively the landmark and iterative closest point methods for registration of CT and MR images of the prostate gland after placement of fiducial markers. The study was approved by the institutional ethics review board, and informed consent was obtained. CT and MR images were registered by using fiducial gold markers that were inserted into the prostate. Two image registration methods—a commonly available landmark method and dedicated iterative closest point method—were compared. Precision was assessed for a data set of 21 patients by using five operators. Precision of the iterative closest point method (1.1 mm) was significantly better ($P < .01$) than that of the landmark method (2.0 mm). Furthermore, a method is described by which multimodal MR imaging data are reduced into a single interpreted volume that, after registration, can be incorporated into treatment planning.

Radiation therapy for prostate cancer by using intensity-modulated radiation therapy (IMRT) improves the therapeutic ratio by directing an increased uniform dose of radiation to the prostate gland while sparing the surrounding organs (1). If tumor nodules within the prostate or the dominant intraprostatic lesion (DIL) can be localized, then IMRT can be used to escalate the focal dose by delivering a boost dose to the DIL (2). Findings from dose planning studies show that there is an increased probability of tumor control by administering a boost dose to the DIL (3). Designing an IMRT plan requires detailed information about the prostate and DIL. Conventional treatment planning uses the electron density estimate obtained at computed tomography (CT) to calculate dose distribution. CT does not, however, provide good tumor localization and is inaccurate in facilitating discrimination between the base and apex of the prostate and the surrounding structures (4). It is, therefore, clear that prostate IMRT planning requires additional imaging information to attain optimal performance.

Magnetic resonance (MR) imaging can facilitate prostate delineation and tumor (DIL) localization. In 67% of tumors, the location of the tumor can be correctly depicted at high-spatial-resolution T2-weighted MR imaging by using a 1.5-T endorectal coil (5). The addition of findings from proton MR spectroscopic imaging results in a 90% sextant positive predictive value (6). Findings from multisection fast dynamic contrast material–enhanced MR imaging can also provide additional information (7,8). The combination of data from T2-weighted MR imaging, dynamic contrast-enhanced MR imaging, and MR spectroscopic imaging has been previously shown to provide up to 93% localization accuracy (9). Thus, tumor localization with MR imaging appears to be at a level that is suitable for use with IMRT planning.

Integration of MR imaging with IMRT treatment planning requires good alignment (registration) of CT and MR images. A common approach to image registration uses the correlation between gray values obtained at CT and those obtained

at MR imaging (eg, normalized mutual information [10]). Poor visualization of the prostate at CT and the difference in prostate size with respect to MR imaging (4), however, render the mutual registration of MR imaging and CT information inaccurate, if not unreliable. Bone landmark methods are quick and reliable but do not account for prostate movement (11). In this study, we had the opportunity to use intraprostatic fiducial gold markers. These markers are already used for correcting prostate position during all fractions of IMRT (12) because the markers do not migrate (13). These intraprostatic fiducial markers were previously used to register CT and MR images (14), although, to the best of our knowledge, the registration error of this technique has not been studied. Furthermore, the authors (14) used a readily available manual single point landmark technique. We hypothesize that registration errors can be significantly decreased by using a surface registration technique. Thus, the purpose of our study was to compare prospectively the landmark and iterative closest point (ICP) methods for registration of CT and MR images of the prostate gland after placement of fiducial markers.

Materials and Methods

Patients

The data set in this study was obtained between September 2001 and June 2002 for 21 consecutive patients who had histologically proved prostate cancer and who were scheduled for radiation therapy. The patients underwent CT and MR imaging within 1 week. Mean prostate specific antigen level was 15.1 ng/mL (range, 6.0–27.0 ng/mL), and median Gleason score was 6 (range, 4–10). Seven of the 21 patients demonstrated non–organ-confined disease (stage T3a or higher), and 14 demonstrated organ-confined disease (stage T2b or lower); tumor stage was determined on the basis of the TNM classification. No hormone treatment was administered between MR and CT examinations.

At least 2 weeks prior to imaging, an experienced urologist (J.A.W., 10 years of experience in urology) inserted four 1 × 7-mm gold markers by using transrectal ultrasonographic guidance. Two markers were inserted in the base of the prostate, one in the apex of the prostate, and one in the central portion of the prostate. Patient positioning—supine on a flat couch, with foam knee support—was identical for both CT and MR imaging. This study was approved by the institutional ethics review board, and informed consent was obtained.

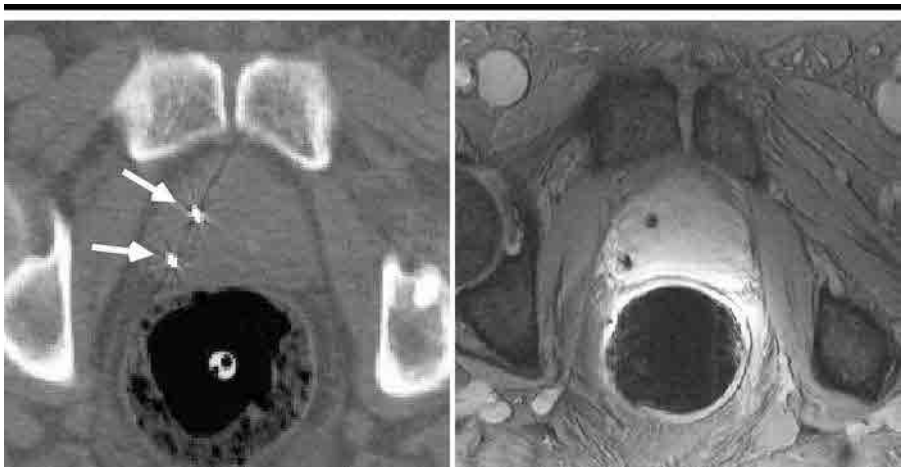

Figure 1. Transverse CT (left) and T2*-weighted MR (right) images (see Table 1 for MR imaging parameters) before image registration. Markers appear as bright spots at CT (arrows) and as dark spots at MR imaging.

Data Acquisition

The CT volume that was used for IMRT planning was acquired with a multisection CT scanner (AcQsim; Marconi Medical Systems, Cleveland, Ohio) (3-mm collimation, 150 mA, 140 kV, and 12.5-mm table feed per 0.5-second scanner rotation). In 11 patients, an endorectal balloon was inserted and inflated with 80 mL of air to mimic MR imaging conditions and possibly to reduce prostate deformation differences. The endorectal balloon that was used at CT was a modified MR imaging balloon (MedRad, Pittsburgh, Pa) without the coil wiring.

MR imaging was performed by using a 1.5-T whole-body imaging system (Magnetom Sonata; Siemens, Erlangen, Germany). Patients were imaged in the supine position by using an integrated endorectal pelvic phased-array coil (Siemens). After the digital rectal examination, the endorectal coil (Medrad) was inserted and inflated with 80 mL of air. Peristalsis was suppressed by means of an intramuscular injection of 1 mg glucagon (Glucagen; Novo Nordisk, Bagsvaerd, Denmark) before the examination. Localization images were acquired to determine anatomic orientation and to confirm coil positioning.

MR imaging parameters are summarized in Table 1. Transverse T2*-weighted gradient-echo MR imaging provided clear visualization of the gold markers. T2-weighted spin-echo MR imaging in three perpendicular planes provided detail of the in-plane anatomy. Metabolic information was obtained by using 3D spectroscopic imaging (15,16). Contrast-enhanced functional MR imaging was performed in two interleaved modes: high-spatial-resolution mode and fast mode. Both modes comprised repeated T1-weighted MR imaging sequences and one intermediate-weighted MR imaging sequence. The imaging order prior to contrast material administration is presented in Table 1. After contrast material administration, 74 dynamic T1-weighted fast 3D gradient-echo and five dynamic T1-weighted high-resolution 3D gradient-echo MR imaging sequences were performed. A dose of 0.2 mmol per kilogram body weight of gadopentetate dimeglumine (Magnevist; Schering, Berlin, Germany) was injected by using a power injector (Spectris; Medrad) with saline flush.

Image Registration Methods

CT and MR image sets (Fig 1) were aligned by registering the CT volume with the transverse T2*-weighted MR imaging volume. Two image registration methods were applied. The first was a current and widely available landmark-based method. The second was a surface-based ICP method. The registration transform was limited to a rigid body transform (three translation and three rotation parameters).

For the landmark-based method, the operator collected pairs of conjugate points. Each pair corresponded to the midpoint of the same fiducial marker on CT and MR images. A registration (ie, a set of six rigid body parameters) that minimized the root-mean-square distance between these point pairs was then determined (17).

The ICP-based method entailed a man-

TABLE 1
Imaging Parameters for MR Imaging and Spectroscopy

Modality	Imaging Order*	Repetition Time (msec)	Echo Time (msec)	No. of Echoes	No. of Signals Acquired	Flip Angle (degrees)	Section Thickness (mm)	Matrix	No. of Sections	Field of View (mm)	Phase-encoding Direction	Dynamic Volume Sampling Time (sec)
MR imaging												
Transverse T2*-weighted gradient-echo	2	700	18	1	2	30	3	512 × 448	22	285	Column	NA
T2-weighted spin-echo	1	3500	132	15	2	180	5	240 × 512	11–22	280	Row	NA
Intermediate-weighted high-resolution 3D gradient-echo	3	30	4	1	1	10	2.5	512 × 256 × 18	NA	280	Column	NA
Dynamic T1-weighted high-resolution 3D gradient-echo	4	8.2	4	1	2	20	2.5	512 × 256 × 18	NA	280	Column	90
Intermediate-weighted fast 3D gradient-echo	5	800	1.6	1	1	8	4	256 × 77 × 10	NA	280	Column	NA
Dynamic T1-weighted fast 3D gradient-echo	6	34	1.6	1	1	14	4	256 × 77 × 10	NA	280	Column	2
MR spectroscopic imaging												
3D point-resolved proton spectroscopy with band-selective inversion with gradient dephasing	. . .	650	120	NA	8	NA	8	12 × 12 × 12	NA	96	NA	NA

Note.—NA = not applicable.
* One of each sequence was performed prior to contrast material administration. After contrast material administration, 74 dynamic T1-weighted fast 3D gradient-echo and five dynamic T1-weighted high-resolution 3D gradient-echo MR imaging sequences were performed.

ual segmentation of the markers. Segmentation was performed by using an open-source software program (3D Slicer, versions 1.2 and 1.3; *www.slicer.org*). The CT and MR marker segmentations were each converted into a surface model. A registration of the CT and MR marker models that would minimize the root-mean-square distance between the surfaces by using the ICP method was then determined (18).

The registration was visually inspected by observing the fused CT and MR image. MR features were depicted in gray, and CT features were fused in red, with the CT window width and window level set to reveal only the markers (Fig 2). If the fused image demonstrated misregistrations that were clearly visible, the registration procedure was reiterated.

Each CT and MR image pair was registered by three or four operators from a group of two radiologists, three physicists, and one radiation oncologist (J.J.F., A.W., H.J.H., J.A.v.D., and E.N.J.T.v.L., none of whom had previous experience in landmark and ICP image registration). Five operators repeated the registrations up to five times in five patients. The amount of time needed to perform registration was estimated by one operator (H.J.H.) by using a stopwatch in 10 patients for both methods. Computing time was estimated by using software that was built in our institution (H.J.H.) and a personal computer (Intel Pentium III [650-MHz]; Dell, Round Rock, Tex).

Functional Image Postprocessing

Postprocessing entailed two stages. First, the acquired dynamic and spectroscopic data were processed to extract several functional and feature images. Second, T2-weighted MR images and dynamic contrast-enhanced MR and 3D spectroscopic feature images were further reduced into a single map.

The 3D spectroscopic citrate and choline image volumes were calculated by using a workstation software program (Syngo; Siemens). This software implements filtering, zero filling, and spectral fitting of citrate and choline peaks (19). For tumor localization, a derived feature—that is, the choline to citrate ratio—was used (20,21) (Fig 3).

The dynamic image volume data were converted into a tracer concentration by using the intermediate-weighted sequence and the inversion of the sequence signal model (22). Software that was developed in-house was used to fit contrast curves robustly to a physiologic compartment model (23,24), and the model parameters were calibrated by using a reference tissue method (25). Examples of physiologic features were extracellular volume, surface area permeability in low flow regions, volume transfer constant, and arrival time. Examples are shown in Figure 3.

The feature images were transparently overlaid in color onto the T2-weighted MR images in three perpendicular planes. A built-in 3D editor was used to delineate the tumor boundary. During editing, the operator switched between the feature images, with the cross section of the tumor model visible in all planes. The tumor model was then saved as a tumor image map. The registration parameters that aligned the transverse T2*-weighted MR images with CT data were used to align the tumor map with CT data. The aligned tumor map was then transferred to the radiation therapy department and used in the IMRT planning (Fig 4).

Statistical Analysis

Each registration resulted in a six-parameter (rigid) transform. To compare the registration results, each six-parameter transform was applied to two fixed target locations within a patient. The first target location was the marker centroid, which was estimated from the average of the segmented points on transverse T2*-weighted MR images for each registration

method. The second target location was a simulated prostate rim point, which was determined by translating 20 mm left, 20 mm anterior, and 20 mm caudal from the estimated marker centroid.

The location of the centroid and rim targets could not be compared directly between patients to assess registration performance. Therefore, a target error vector was determined as follows: For each patient, registration method, and target, the average target location was subtracted from a target location. This can be regarded as a biased estimate of the target error. Because the number of registrations per patient per method was rather low (on the order of three to four registrations), a trimmed (25% symmetric) mean method was used to determine the least biased average.

The squared length of the target error vectors is a measure of the precision and follows a χ^2 distribution (17). The χ^2 distribution is characterized according to a mean and standard deviation. Again, robust estimates were used. The mean was estimated by using a trimmed (25% symmetric) mean method. The average standard deviation was estimated by using the median of the absolute deviation method. The standard deviation of the landmark and ICP methods was compared by using the nonparametric Wilcoxon test. An analysis of variance test was used to analyze the influence of different factors (inter- and intraoperator characteristics and balloon presence) on target error. All statistical methods were validated by conducting additional tests on data sets with known Gaussian distributions. All statistics were performed by using a statistical software package (R, version 5.1) (26). For all statistical tests, a *P* value of less than .01 was considered to indicate a statistically significant difference.

Results

The operators performed a total of 179 registrations. An experienced operator was able to segment the fiducial markers in both modalities in an average of 5 minutes with the ICP method; segmentation of fiducial markers required 2 minutes with the landmark method. The computing time that was required to find the optimum registration was on the order of seconds.

The ICP method was significantly more precise than the landmark method ($P < .01$). This is graphically demonstrated in Figure 5, which presents the distribution of target error lengths for the two registration transforms at the two target locations. As anticipated, the precision was much better at the centroid than at the rim. The target error distributions are further summarized in Table 2. The average precision of the ICP method was significantly better than that of the landmark method ($P < .01$). Table 3 summarizes the number of registrations that had a rim target error larger than 2 or 5 mm, where 2 mm is the clinical goal and 5 mm can be regarded as an upper limit of acceptability. More than half of the landmark registrations had a target error that was larger than the clinical limit. The landmark method also yielded a substantial amount of unacceptable registrations. Neither the operator nor the presence of an endorectal balloon had a statistically significant effect on the registration error ($P > .01$).

For one patient, the DIL was outlined in consensus by expert radiologists (J.J.F., J.O.B.) by using our MR contrast analysis and evaluation package that was developed in-house and the whole-body imaging data previously described in the Materials and Methods. The outline of the DIL was carefully positioned according to information from T2-weighted MR images and dynamic contrast-enhanced MR and 3D spectroscopic feature images (Fig 3). The outline surface was converted into an image volume label map. The label map was resampled and transformed into the CT domain by using the ICP-obtained registration parameters. The CT-format tumor map was then communicated to the radiation therapy department by using the standard Digital Imaging and Communications in Medicine protocol. The intention of the IMRT plan was to deliver a uniform dose of 70 Gy to the whole prostate gland and a boost dose of 90 Gy to the DIL, as shown in Figure 4.

Discussion

We were able to confirm the postulated hypothesis that registration with a manually segmented marker surface (ICP method) is significantly more precise than registration with a manually picked marker center (landmark method) (Table 2). This is in agreement with landmark registration theory on the effect of fiducial marker localization error (17). As has also been observed by Parker et al (14), the user-defined fiducial marker surface in the ICP method provides better spatial information than the single user-defined fiducial marker center in the landmark method. Our study thus demonstrates that the localization of fiducial markers is important in the registration of CT and MR images for radiation therapy treatment planning of the prostate.

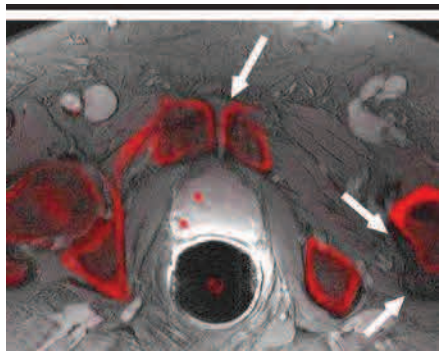

Figure 2. Fused display of transverse T2*-weighted MR (gray value) and CT (red overlay) images for validation of registration (see Table 1 for MR imaging parameters). CT markers overlay transverse T2*-weighted markers completely, which confirms good prostate registration. Notice bone landmark shift (arrows) illustrating inability to register prostate by using bone landmarks.

We have assessed the precision and have demonstrated that, in our study, the ICP method can be regarded as clinically acceptable because 86% of ICP registrations had a precision better than 2 mm at the rim of the prostate, whereas only 42% of landmark registrations had a precision better than 2 mm at the rim of the prostate. Image registration will never be perfect; image noise, spatial resolution, and many other factors impose a lower limit on the achievable registration error. Findings from this study clearly demonstrate that the actual achievable performance varies markedly between the registration methods that are available either in literature or on commercial systems. Determining the performance of registration methods is therefore important for choosing between methods or even for deciding on the acceptability.

To be clinically useful, the image registration target error should not be larger than the IMRT treatment error. An analysis of the geometric variations during treatment by using offline position correction indicates that the overall systematic error (1 standard deviation) is approximately 1.5 mm (27,28), and the random variations range from 2.8 to 4.4 mm (1 standard deviation) in the three orthogonal directions. Choosing 2.0 mm (1 standard deviation) as an upper limit for the image registration target error limits the overall systematic error increase to

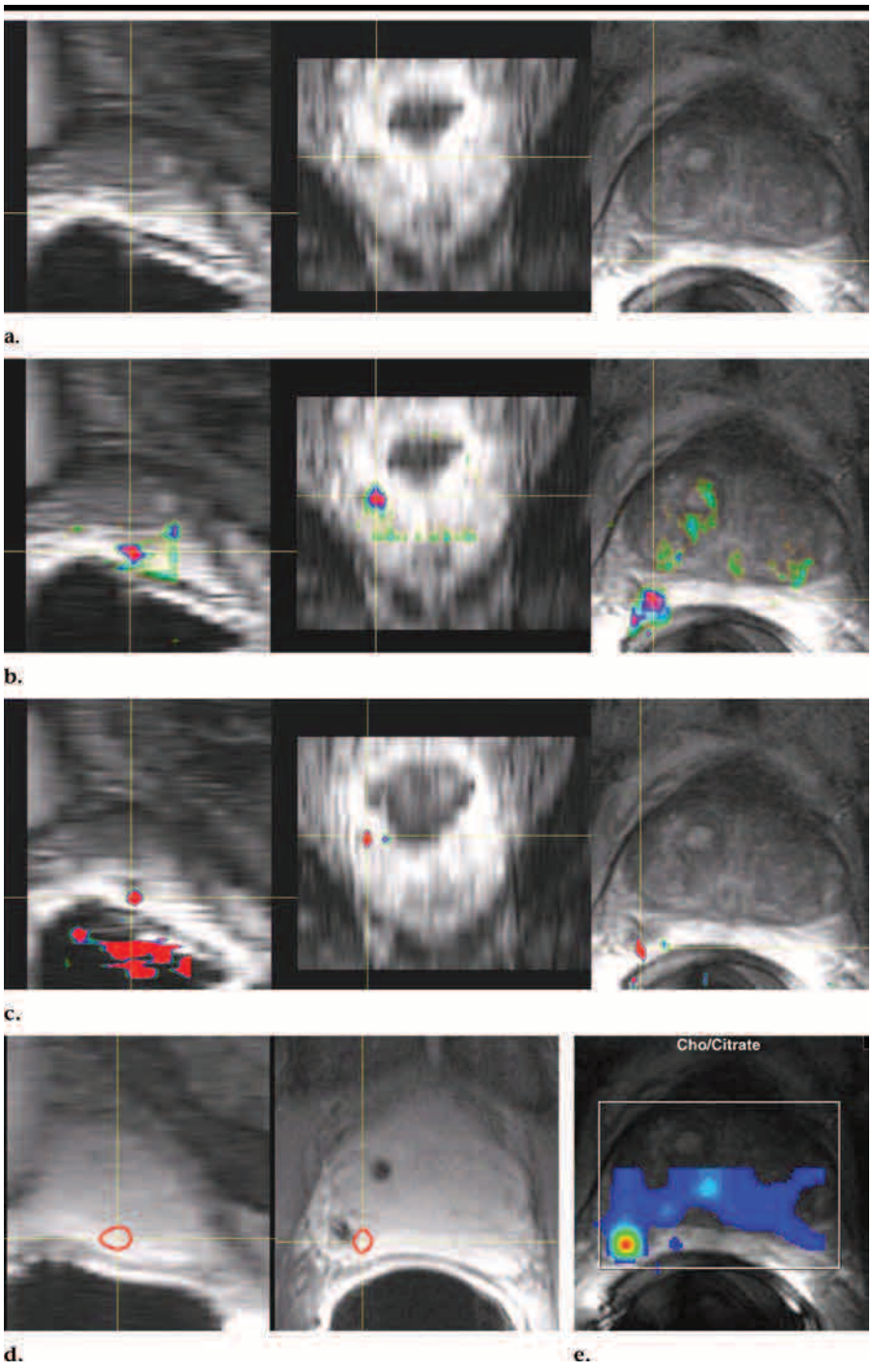

Figure 3. Images show integration of T2-weighted MR, dynamic contrast-enhanced MR, and 3D spectroscopic image information into a single tumor map (see Table 1 for MR imaging parameters). **(a)** T2-weighted MR image shows hypointense area in sagittal (left), coronal (center), and transverse (right) position fused with **(b)** volume transfer constant, **(c)** wash-out phase, and **(d)** choline-to-citrate ratio (see body text for explanation of parameters), all of which confirm DIL position. **(e)** Red DIL outline is visualized according to its cross section.

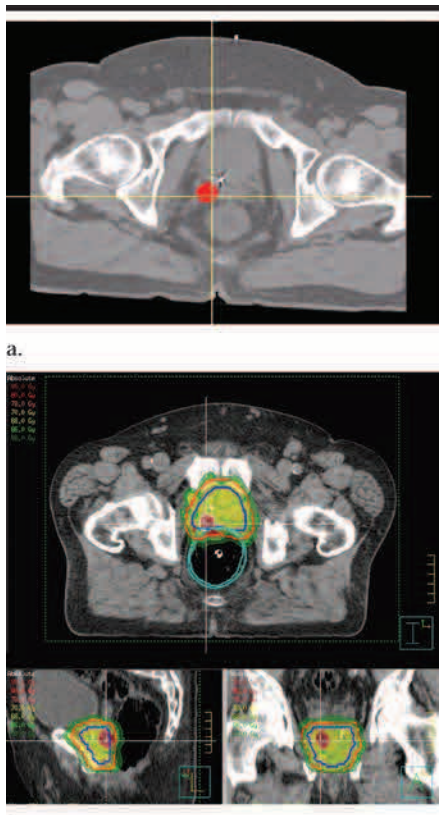

Figure 4. Images show **(a)** registered tumor map overlaid in red on top of transverse treatment-planning CT image and **(b)** radiation therapy treatment plan. Notice how boost dose area conforms to DIL area demonstrated at MR imaging.

1.0 mm (1 standard deviation). This is also typical for the geometric error allowed in treatment planning and dose delivery of IMRT (29).

The proposed ICP-based method met the needs for this study; however, opportunities are present for improvement. The manual segmentation process is elaborate. Automatic segmentation, possibly incorporating prior knowledge regarding the fiducial marker shape, will reduce the time required for image segmentation and is likely to further decrease fiducial marker localization errors (30). Given the results of the current study, it seems worthwhile to investigate such automatic fiducial marker detection strategies. A related topic of study is the number and size of the fiducial markers (31). Our assumption that the intrastudy prostate movements were negligible also requires improvements. Currently, a manual correction can be performed by overlaying the images and shifting the drawing area. Future implementations of our software will be extended with rigid intermodality registration methods to reduce effects of intrastudy prostate movement.

The evaluation method used in this study (17) assumes that fiducial markers do not move relative to each other. This assumption is valid for multimodality brain image registration, the technique for which this method was developed, but this assumption is possibly not true

for prostate image registration. Although marker migration is assumed to be low (13), a real estimate is required. We are currently researching techniques to extend the evaluation method to include migration and deformation effects.

Our results did not demonstrate that the presence of an endorectal balloon had an effect on the registration precision. It is expected, however, that the presence of an endorectal balloon affects the shape of the prostate. Thus, for clinical application, we will continue to use the balloon with CT. We are also aware of nonrigid registration techniques that may compensate for such prostate deformation. Nonrigid fiducial marker-based techniques would require a much denser fiducial marker sampling of the prostate, which then becomes clinically unacceptable. And, as we have already stated, gray value registration is not an option. Moreover, assessing the registration errors of nonrigid registration techniques is a terra incognita. We are not aware of demonstrably accurate and precise nonrigid registration techniques for matching CT and MR images of the prostate.

Findings from this study demonstrate how MR imaging information can be provided to a radiation therapy department for integration in the treatment plan. First, the anatomic, functional, and metabolic MR features are integrated into a single tumor map. Second, this map is registered to treatment CT images. Tumor localization performance will obviously have an effect on the total achievable error that is associated with this tumor map. We and other groups have already demonstrated the feasibility of tumor localization (6,9) and are actively researching improvements. Our robust and calibrated contrast enhancement features (23,24) already facilitate multicenter trials. Furthermore, we expect that computer-aided diagnosis techniques can enhance diagnostic performance.

A limitation of the current study design is that it does not account for systematic errors in the fiducial marker localization. Such errors may occur as the result of asymmetries in the imaging modality or segmentation process. Because CT is the reference modality for the IMRT treatment plan, it is the MR imaging asymmetries that are of interest. Parker et al (14) estimated that the fiducial marker-induced MR asymmetry was less than 1 mm. Furthermore, the fiducial marker localization methods we applied are visually symmetric. Looking for the center or segmenting opposite sides of a fiducial marker is not likely to introduce asymmetry artifacts. We therefore conclude that, in our study design, the total registration error will be only marginally larger than the precision-derived estimate.

In conclusion, precise alignment of CT and MR images of the prostate is possible by using fiducial gold markers and dedicated registration methods. A functional MR analysis tool is required that can reduce multiple functional MR imaging parameters into a single interpreted prostatic lesion map. The registered lesion map allows a radiologist to provide the radiation oncologist with the information required to design an IMRT treatment plan. Integrated multimodal functional MR imaging information can be included in radiation therapy treatment planning for prostate cancer by using precise alignment of fiducial gold markers.

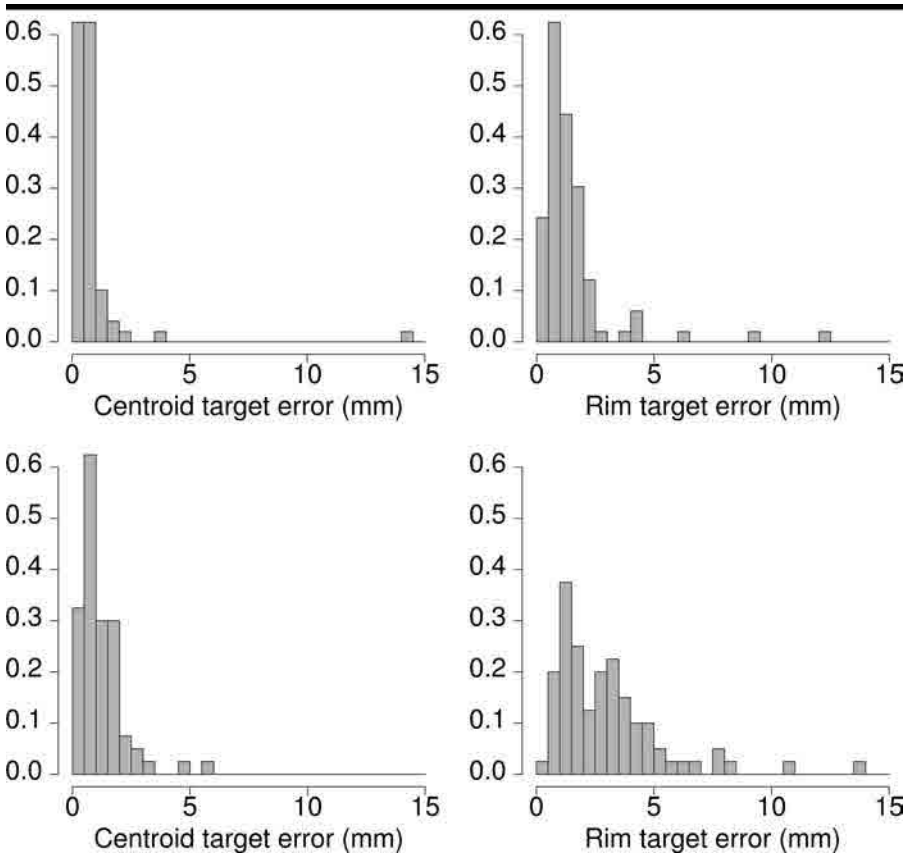

Figure 5. Bar graphs demonstrate relative frequency (y axis) of prostate registration errors (x axis) for ICP (top graphs) and landmark (bottom graphs) registration methods at centroid (left graphs) and rim location (right graphs). Notice broader error distribution for landmark method.

TABLE 2
Summary of Prostate Image Registration Errors at Centroid and Rim

	Centroid		Rim	
Registration Method	Mean (mm)	Standard Deviation	Mean (mm)	Standard Deviation
Landmark	0.9	0.6	2.5	1.9
ICP	0.5	0.3	1.1	0.7

TABLE 3
Predicted Number of Registrations That Have an Estimated Rim Target Error Larger than 2 or 5 mm

Registration Method	Target Error > 2 mm	Target Error > 5 mm
Landmark	46/80 (58)	10/80 (13)
ICP	14/99 (14)	3/99 (3)

Note.—Numbers in parentheses are percentages.

References

1. Zelefsky MJ, Fuks Z, Hunt M, et al. High dose radiation delivered by intensity modulated conformal radiotherapy improves the outcome of localized prostate cancer. J Urol 2001; 166:876–881.
2. Pickett B, Vigneault E, Kurhanewicz J, Verhey L, Roach M. Static field intensity modulation to treat a dominant intra-prostatic lesion to 90 Gy compared to seven field 3-dimensional radiotherapy. Int J Radiat Oncol Biol Phys 1999; 44:921–929.
3. Nutting CM, Corbishley CM, Sanchez-Nieto B, Cosgrove VP, Webb S, Dearnaley DP. Potential improvements in the therapeutic ratio of prostate cancer irradiation: dose escalation of pathologically identified tumour nodules using intensity modulated radiotherapy. Br J Radiol 2002; 75:151–161.
4. Rasch C, Barillot I, Remeijer P, Touw A, van Herk M, Lebesque JV. Definition of the prostate in CT and MRI: a multi-observer study. Int J Radiat Oncol Biol Phys 1999; 43:57–66.
5. Jager GJ, Ruijter ET, van de Kaa CA, et al. Local staging of prostate cancer with endorectal MR imaging: correlation with histopathology. AJR Am J Roentgenol 1996; 166:845–852.
6. Scheidler J, Hricak H, Vigneron DB, et al. Prostate cancer: localization with three-dimensional proton MR spectroscopic imaging—clinicopathologic study. Radiology 1999; 213:473–480.
7. Engelbrecht MR, Huisman HJ, Laheij RJ, et al. Discrimination of prostate cancer from normal peripheral zone and central gland tissue by using dynamic contrast-enhanced MR imaging. Radiology 2003; 229: 248–254.
8. Padhani AR, Gapinski CJ, Macvicar DA, et al. Dynamic contrast enhanced MRI of prostate cancer: correlation with morphology and tumour stage, histological grade and PSA. Clin Radiol 2000; 55:99–109.
9. Fütterer JJ, Scheenen TWJ, Welmers A, De la Rosette JJMC, Blickman JG, Barentsz JO. Dynamic contrast-enhanced MRI using both high spatial and high temporal resolution combined with 3D-MR spectroscopy in prostate cancer imaging (abstr). Radiology 2002; 225(P):628.
10. Studholme C, Hill D, Hawkes D. An overlap invariant entropy measure of 3D medical image alignment. Pattern Recognition 1999; 32:71–86.
11. van Herk M, Bruce A, Kroes AP, Shouman T, Touw A, Lebesque JV. Quantification of organ motion during conformal radiotherapy of the prostate by three dimensional image registration. Int J Radiat Oncol Biol Phys 1995; 33:1311–1320.
12. Alasti H, Petric MP, Catton CN, Warde PR. Portal imaging for evaluation of daily online setup errors and off-line organ motion during conformal irradiation of carcinoma of the prostate. Int J Radiat Oncol Biol Phys 2001; 49:869–884.
13. Pouliot J, Aubin M, Langen KM, et al. (Non)-migration of radiopaque markers used for on-line localization of the prostate with an electronic portal imaging device. Int J Radiat Oncol Biol Phys 2003; 56:862–866.
14. Parker CC, Damyanovich A, Haycocks T, Haider M, Bayley A, Catton CN. Magnetic resonance imaging in the radiation treatment planning of localized prostate cancer using intra-prostatic fiducial markers for computed tomography co-registration. Radiother Oncol 2003; 66:217–224.
15. Scheenen TW, Klomp DW, Roll SA, Futterer JJ, Barentsz JO, Heerschap A. Fast acquisition-weighted three-dimensional proton MR spectroscopic imaging of the human prostate. Magn Reson Med 2004; 52: 80–88.
16. Kurhanewicz J, Vigneron DB, Hricak H, Narayan P, Carroll P, Nelson SJ. Three-dimensional H-1 MR spectroscopic imaging of the in situ human prostate with high (0.24-0.7-cm^3) spatial resolution. Radiology 1996; 198:795–805.
17. Fitzpatrick JM, West JB, Maurer CR. Predicting error in rigid-body point-based registration. IEEE Trans Med Imaging 1998; 17:694–702.
18. Besl P, McKay N. A method for registration of 3D shapes. IEEE Trans Pattern Analysis Machine Intelligence 1992; 18:239–256.
19. van der Graaf M, van den Boogert HJ, Jager GJ, Barentsz JO, Heerschap A. Human prostate: multisection proton MR spectroscopic imaging with a single spin-echo sequence—preliminary experience. Radiology 1999; 213:919–925.
20. Heerschap A, Jager GJ, van der Graaf M, et al. In vivo proton MR spectroscopy reveals altered metabolite content in malignant prostate tissue. Anticancer Res 1997; 17: 1455–1460.
21. Kurhanewicz J, Swanson MG, Wood PJ, Vigneron DB. Magnetic resonance imaging and spectroscopic imaging: improved patient selection and potential for metabolic intermediate endpoints in prostate cancer chemoprevention trials. Urology 2001; 57:124–128.
22. Hittmair K, Gomiscek G, Lanenberger K, Recht M, Imhof H. Method for the quantitative assessment of contrast agent uptake in dynamic contrast-enhanced MRI. Magn Reson Med 1994; 31:567–571.
23. Huisman HJ, Engelbrecht MR, Barentsz JO. Accurate estimation of pharmacokinetic contrast-enhanced dynamic MRI parameters of the prostate. J Magn Reson Imaging 2001; 13:607–614.
24. Tofts PS, Brix G, Buckley DL, et al. Estimating kinetic parameters from dynamic contrast-enhanced T(1)-weighted MRI of a diffusable tracer: standardized quantities and symbols. J Magn Reson Imaging 1999; 10: 223–232.
25. Kovar DA, Lewis M, Karczmar GS. A new method for imaging perfusion and contrast extraction fraction: input functions derived from reference tissues. J Magn Reson Imaging 1998; 8:1126–1134.
26. Ihaka R, Gentleman R. R: a language for data analysis and graphics. J Comput Graph Stat 1996; 5:299–314.
27. van Lin EN, Nijenhuis E, Huizenga H, van der Vight L, Visser A. Effectiveness of couch height-based patient set-up and an off-line correction protocol in prostate cancer radiotherapy. Int J Radiat Oncol Biol Phys 2001; 50:569–577.
28. Litzenberg D, Dawson LA, Sandler H, et al. Daily prostate targeting using implanted radiopaque markers. Int J Radiat Oncol Biol Phys 2002; 52:699–703.
29. Partridge M, Symonds-Tayler JR, Evans PM. IMRT verification with a camera-based electronic portal imaging system. Phys Med Biol 2000; 45:183–196.
30. Nederveen A, Lagendijk J, Hofman P. Detection of fiducial gold markers for automatic on-line megavoltage position verification using a marker extraction kernel (MEK). Int J Radiat Oncol Biol Phys 2000; 47:1435–1442.
31. Maurer CR Jr, Fitzpatrick JM, Wang MY, Galloway RL Jr, Maciunas RJ, Allen GS. Registration of head volume images using implantable fiducial markers. IEEE Trans Med Imaging 1997; 16:447–462.